A98-31507

ICAS-98-2,5,1

SIMULATION OF FLUID STRUCTURE INTERACTION AT THE HELICOPTER ROTOR

K-H Hierholz[*], S. Wagner[†]
Institute of Aerodynamics and Gasdynamics (IAG), University of Stuttgart, Germany

Abstract

An approach for the numerical simulation of the aeroelastic behaviour of a multiblade helicopter rotor in hover and forward flight is presented. To describe the compressible, unsteady and transonic flow in forward flight the 3-D Finite-Volume Euler CFD Code INROT with a chimera overlapping embedded grid technique is used. It is coupled with a structural dynamic model which provides blade movement and deformation. The solution of the coupled problem is found through a staggered procedure in which the two fields are integrated in time. After each time step, the positions and velocities of the structural domain and the surface pressure of the fluid domain are exchanged. An efficient 3-D dynamic grid algorithm as well as a geometric conservative formulation of the Euler Equations for dynamic grids have been implemented. First results of coupled calculations are shown for the 5-bladed Hughes-500 Rotor in hover and in 100 kt forward flight.

1 Introduction

A helicopter rotor in forward flight is a complex and strongly coupled aerodynamic-dynamic system. The interaction of airloads and rotor dynamics determines the flight mechanics and stability of the helicopter. Blade vortex interaction, the interaction of the blade with the tip vortex system, and to a smaller extent, with the root vortex system have a strong influence on vibration and noise production under some critical flight conditions like slow descent.

Future helicopters will have to meet higher requirements in terms of vibration and noise level in ever shorter development times. Therefore it is necessary to achieve a deeper insight into the physical processes through experimental investigation and numerical simulation. As we are dealing with a strongly coupled interdisciplinary problem, the simulation models for the fluid and structural domains must be sufficient accurate to reflect on the one hand the relevant physical phenomena in each domain. On the other hand, the coupled model must reflect the interaction of the surface-coupled problem with sufficient accuracy. The first point demands a modular design, allowing the use of the elaborate methods already developed for the fluid and structural domains, where new experience and model refinements may easily be incorporated in each of the two domains. The second point calls for the use of a sufficiently tight coupling scheme to meet the stability and accuracy requirements of the coupled problem.

The flow field at the rotor is compressible, transonic, 3-D and highly unsteady. Within a few fractions of a second, the blade will move from the advancing side with small angles of attack, transonic flow and possible shocks to the retreating side with low dynamic pressure, high angles of attack and viscous-dominated flow with possible dynamic stall. The CFD methods used to describe the flow field with different degrees of abstraction are reaching from the blade-element theory over potential methods and the transonic small disturbance (TSD) methods to the Euler and Navier-Stokes methods. The dynamic behaviour of the rotor system is determined by the elasticity properties of the blades as well as by the design of the rotor hub. The multibody simulation methodology appropriately represents this complex system where multiple bodies are kinematically connected by hinges. Different degrees of accuracy may be achieved by using rigid bodies only, elastic beam elements with bending and torsional degrees of freedom, a FEM beam structure or a 3-D FEM-structure model for the blades.

Over the last 20 years, the coupling of CFD and structural mechanic techniques e.g. for the aeroelastic analysis of profiles and later for wings and complete aircraft configurations has been developed. Ballhaus and Goorjian [1] used the 2-D TSD-Code LTRAN2 and presented the harmonic analysis technique as well as the time-marching technique for aeroelastic calculations in 1978. Rizetta [25], Guruswamy [11] and Edwards [7] investigated the aeroelastic properties of wing profiles in transonic flow using the TSD-equations. The Euler equations for the aeroelastic analysis of a complete wing were used by Guruswamy [12] in 1988, the Navier-Stokes equations in a "thin-layer" formulation were used for wings in [13, 22]. In 1989, Batina [2] published the unsteady investigation of a complete F-16 Fighter configuration using the TSD Code CAP-TSD, and in 1991 [3] the investigation of a complete aircraft with the Euler equations. An overview of unsteady and aeroelastic methods is given by Edwards and Malone [8] and by Kutler [14].

Investigations and classifications concerning Euler and Navier-Stokes methods on deforming grids, of the properties of staggered solution coupling schemes may be found in [9, 10, 23, 24, 28, 19]. Investigations concerning the geometric conservation law may be found in [27, 5, 29, 31, 21, 17, 19].

2 Method Applied

In the present approach, the flow field is described by the unsteady 3-D Finite-Volume Godunov-type Euler Code INROT. A cell-centered method is used. The implicit time discretization is second or optionally third order time-accurate. An approximate Riemann solver following Eberle [6] is used for the flux calculation. A UNO (uniformly high order non-oscillatory) scheme is used for the spatial discretization, where the spatial accuracy is of third order, reduced to first order near discontinuities. The code was extended by dynamic 3-D grids and a geometric conservative ALE formulation of the flow equations. For the structural model the multibody simulation tool SIMPACK is used, where the dynamic system is represented by rigid or flexible kinematically connected bodies. In the calculations presented, the rotor blades are modelled as rotating flexible beams with modal bending and torsional degrees of freedom. The solution of the coupled two-field-problem is found by a time-marching staggered solution. Thanks to its modular design, the whole model can switch to a FEM surface discretization without any change in the aerodynamic module or the interface.

2.1 Aerodynamic calculation

The Euler equations are used to model the flow field. They are formulated in a hub-attached, non-inertial rotating frame of reference with centrifugal and coriolis forces included. Krämer [15,16] showed that the use of absolute variables $\overline{v}, \overline{e}$ for velocity and energy avoids the occurrence of systematic numerical errors even in the steady rotating case. To calculate the flow around deforming boundaries, a purely Eulerian description of the flow domain is no longer sufficient, since grid points at the boundary and in the interior of the fluid domain are moving. To handle these grid movements and deformations correctly, we use the Arbitrary-Lagrangian-Eulerian (ALE) formulation of the Euler equations which takes the grid velocities v_g into account [4, 9, 23]. The final differential form of the Euler equations for the rotating moving-grid case in physical coordinates is:

$$\frac{\partial(J\Phi)}{\partial t}\bigg|_{\bar{\xi}} + J\nabla F = JK \tag{2.1}$$

with the absolute velocity in the rotating system

$$\overline{\mathbf{v}} = \mathbf{v} + \begin{pmatrix} 0 \\ 0 \\ \omega \end{pmatrix} \times \mathbf{r} = \begin{pmatrix} u - \omega y \\ v + \omega x \\ w \end{pmatrix} \tag{2.2}$$

with the absolute specific total energy

$$\overline{\overline{e}} = \frac{p}{\kappa - 1} + \frac{1}{2}\rho\overline{v}^2 \tag{2.3}$$

with the solution vector Φ and the RHS-Term K

$$\Phi = \begin{pmatrix} \rho \\ \rho\overline{u} \\ \rho\overline{v} \\ \rho\overline{w} \\ \overline{\overline{e}} \end{pmatrix}, \quad K = \rho\omega \begin{pmatrix} 0 \\ \overline{v} \\ -\overline{u} \\ 0 \\ 0 \end{pmatrix} \tag{2.4}$$

and the convective ALE-flux components

$$F_x = \begin{pmatrix} \rho\,(u - u_g) \\ \rho\overline{u}(u - u_g) + p \\ \rho\overline{v}(u - u_g) \\ \rho\overline{w}(u - u_g) \\ \overline{\overline{e}}(u - u_g) + p\overline{u} \end{pmatrix}, F_y = \begin{pmatrix} \rho\,(v - v_g) \\ \rho\overline{u}(v - v_g) \\ \rho\overline{v}(v - v_g) + p \\ \rho\overline{w}(v - v_g) \\ \overline{\overline{e}}(v - v_g) + p\overline{v} \end{pmatrix}, F_z = \begin{pmatrix} \rho\,(w - w_g) \\ \rho\overline{u}(w - w_g) \\ \rho\overline{v}(w - w_g) \\ \rho\overline{w}(w - w_g) + p \\ \overline{\overline{e}}(w - w_g) + p\overline{w} \end{pmatrix} \tag{2.5}$$

Integrating 2.1 over the cell volume leads to the integral formulation of the Euler equations for one cell. As the physical boundaries of the cell are time dependent, the integration is carried out in the computational domain over $\bar{\xi}$, leading to

$$\int_C \frac{\partial(\Phi J)}{\partial t}\bigg|_{\xi} d\bar{\xi} + \int_C J\nabla F d\bar{\xi} = \int_C JK d\bar{\xi} \tag{2.6}$$

Here, the time derivative can be moved outside the integral as it is taken at constant $\bar{\xi}$, and the cell in computational space is independent of t. Using $d\bar{x} = Jd\bar{\xi}$ and the divergence theorem of Gauss, we finally get:

$$\frac{\partial}{\partial t}\int_C \Phi d\bar{x} + \int_{\partial C} F d\bar{S} = \int_C K d\bar{x} \tag{2.7}$$

The discretized implicit cell-centered finite volume scheme with separate time-discretization of order k used in the current scheme is:

$$\frac{1}{\Delta t}\sum_{m=n+1-k}^{n+1} a^m V^m \Phi^m + \sum_{j=1}^{6} F_j^{n+1}\vec{S}_j^{n+1} = V^{n+1}K^{n+1} \qquad (2.8)$$

1. order in time: $a^{n+1}=1$, $a^n=-1$

2. order in time: $a^{n+1}=\dfrac{3}{2}$, $a^n=-2, a^{n-1}=\dfrac{1}{2}$

3. order in time: $a^{n+1}=\dfrac{11}{6}, a^n=-3, a^{n-1}=\dfrac{3}{2}, a^{n-2}=-\dfrac{1}{3}$

For the solution, the equations are formally transformed from physical into computational space [30]. This transformation is not necessary for a finite volume scheme, since the surface and volume-integrals of the integral conservation equations for each cell can be approximated directly by using geometric surfaces and volumes. The geometric identities of the cell, the normal vectors of cellface triangles and the cell volume are identically used as metrics and the Jacobis. This chosen implementation of the transformation has a formal character and ensures that the discretized integral conservation equations per cell for mass, moment and energy in the physical domain are fulfilled. For the following considerations of geometric conservation, the equations in the physical domain are used.

Discretizing the 5 conservation equations for mass, moment and energy on a moving grid does not automatically lead to a consistent approximation of the fluid flow, because a further condition for the conservation of the volume by the numerical scheme may not be fulfilled. This additional condition is known as "geometric conservation law" (GCL). It can be derived by evaluating the continuity equation of 2.7 for a uniform flow with $\Phi=const, \rho=const$. The ALE fluxes 2.5 can be split into the part due to convection in Eulerian coordinates and the part Φv_g due to the grid motion. The integration of the first constant part over a closed surface gives 0, only the second part contributes to the following result:

$$\frac{\partial}{\partial t}\int_C d\vec{x} + \int_{\partial C} \mathbf{v}_g d\vec{S} = 0 \qquad (2.9)$$

This is a conservation equation for the volume, the time rate of volume change has to be equal to the volume flux due to the moving boundaries. Its discretized form according to 2.8 is:

$$\frac{1}{\Delta t}\sum_{m=n+1-k}^{n+1} a^m V^m + \sum_{j=1}^{6} \mathbf{v}_{g,j}\vec{S}_j^{n+1} = 0 \qquad (2.10)$$

For first order, the sum in the left expression in 2.10 represents the volume change from time step n to n+1. For higher orders, it represents a left side approximation of the volume change. With $(\Delta V)^{n+1}=V^{n+1}-V^n$ it can be expressed as weighted average of volume changes of the last time steps.

$$\frac{1}{\Delta t}\sum_{m=n+2-k}^{n+1} b^m (\Delta V)^m + \sum_{j=1}^{6} \mathbf{v}_{g,j}\vec{S}_j^{n+1} = 0 \qquad (2.11)$$

1. order in time: $b^{n+1}=1$

2. order in time: $b^{n+1}=\dfrac{3}{2}$, $b^n=-\dfrac{1}{2}$

3. order in time: $b^{n+1}=\dfrac{11}{6}, b^n=-\dfrac{7}{6}, b^{n-1}=\dfrac{2}{6}$

k. order in time: $b^m=\sum_{j=m}^{n+1} a^j$, $m \in [n+2-k, n+1]$

Equation 2.11 is the GCL for the implicit, higher time order Finite-Volume-scheme. A numerical scheme which does not respect this condition will not conserve a uniform flow. It can already be seen that the form of the GCL varies with different time discretizations. It will not vary with different flux-approximation methods as long as v_g in the flux calculation is evaluated at the corresponding cell-faces j. The variables in 2.11 are the cell-volume changes in the current and, for higher time orders, in some former time steps, the cellface normal vectors at time $n+1$ due to the implicit formulation, and the grid velocities of the 6 cell-faces. Since the cell-volumes V and their changes as well as the surface normal-vectors are well defined geometric values at every time step, the grid velocity has to be chosen so as to fulfil the GCL 2.11.

This allows a theoretically justified determination of cell-face velocities based only on well known geometrical data, the grid point positions at the actual and some former time steps. This is a very positive effect, since the choice of the appropriate grid velocities without this method is not really evident. It may be chosen at some intermediate time level between n and $n+1$. When the dynamic grid is modelled by a structural mechanic model, e.g. a spring model, the equations of motion for the grid points may also deliver gridpoint velocities at every time-step. But the theoretical justification for the choice of either of the said velocities would remain unsolved.

It may also be noted that the grid velocities occur in the above equations only in the scalar product with the surface-normal-vector as rate of volume change for each cellface, so it is sufficient to determine only the normal component of the cellface-velocity v_g. A remaining problem is, that equation 2.11 does not directly permit a non-ambiguous calculation of the cellface-normal velocities in 3-D. First, we use Hexahedron volume elements, their sides are not necessarily plane. This problem is easily solved by partitioning the cell in 6 tetrahedrons with the Hexahedron volume as sum of the tetrahedron volumes and the surface-normal vectors as sum of two triangle-normal vectors. Second, 2.11 is only one equation for 6 unknown normal velocities, the sum of volume change by the sweeping cellsurfaces must be

equal to a time-averaged volume change of the whole cell, calculated by the first term of 2.11. A direct calculation of v_g based on local cell data and avoiding a LGS over the whole computational domain requires a consistent partitioning of the cell-volume change into 6 cellface-volume changes or 12 volume changes for the surface-triangles of the Hexahedron.

One possibility to get consistent sweep volumes for a surface triangle moving from position at timestep n to its position at timestep $n+1$ is given in [31, 9]. A parametrization for the surface-points as function of 2 spatial parameters and an independent time parameter is used. With this parametrization, the volume overswept by the moving triangle may be integrated exactly. The non-planar sides of the resulting volume are characteristic for this approach, where all 3 corner points of the triangle are moved simultaneously.

For regular Hexahedron grids, it is also possible to construct consistent sweep volumes geometrically using a hexahedron-partitioning into 6 tetrahedrons. Constructing the cell and the swept-over volumes at the cellfaces out of tetrahedrons and proving that all consistency conditions are met would be tedious. But it is possible to use a special class of Hexahedron partitioning both for the cell itself and for the volumes overswept by each cell face. This allows the cell volume and the per-side volume changes to be calculated geometrically with the same formula, while applying some corner-index changes to account for different orientations of the Hexahedron symmetry axis. The corner indices and the Hexahedron partitioning used are shown in the following figure, the tetrahedron connectivity list is {1248}, {1438}, {1378}, {5781}, {5861}, {1286}.
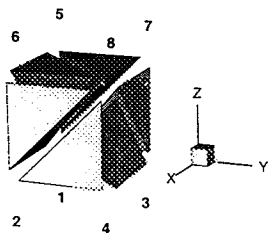

Figure 1: Corner numeration and hexahedron partitioning

This type of partitioning has some characteristic properties, which will allow a simple proof of the consistency conditions. It has only one spatial diagonal in the hexahedron from corner 1 to 8. Its direction (1, 1, 1) also defines the axis of rotational symmetry in computational space for the partitioned hexahedron. Because of this rotational symmetry, the direction of the spatial axis is sufficient to determine the positions and orientations of all tetrahedrons. The surface-diagonal

directions of the Hexahedron are found by projecting the spatial diagonal in ξ, η, and ζ direction to the corresponding front and rear surfaces. This implies directly that the surface diagonal directions of two opposite hexahedron surfaces have the same orientation. When using only hexahedrons of this class with the same symmetry axis orientation, this property ensures the same representation of non-planar surfaces when viewed from the left and right neighbouring cells.

In the moving grid case let us move the hexahedron {1,2,3,4,5,6,7,8} with the spatial diagonal {1,8} to its new position {1',2',3',4',5',6',7',8'}. Consistent sweep volumes per side may now be calculated using the hexahedron-partitioning presented with spatial diagonals according to the following table.

Surface	Hexahedron corners	Spatial diagonal
$\xi=0$	{1',5',3',7',1,5,3,7}	{1',7}
$\eta=0$	{1',2',5',6',1,2,5,6}	{1',6}
$\zeta=0$	{1',3',2',4',1,3,2,4}	{1',4}
$\xi=1$	{2',6',4',8',2,6,4,8}	{2',8}
$\eta=1$	{3',4',7',8',3,4,7,8}	{3',8}
$\zeta=1$	{5',7',6',8',5,7,6,8}	{5',8}

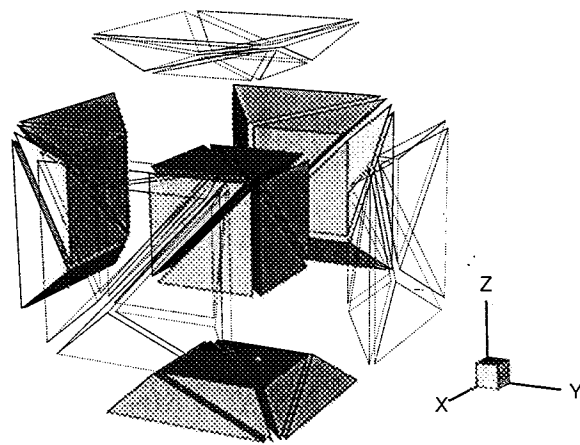**Table 1:** Consistent hexahedron partitioning of the volumes swept over by moving cellfaces

Figure 2: Consistent partitioning of the volumes swept over by moving cellfaces

It is interesting to note that with the above construction, one again has a case of rotational symmetry in computational space, where point 1' is the common starting point for the spatial diagonals of the first 3 sweep-hexahedrons, and point 8 is the common point of the last 3 sweep-hexahedrons.

The local consistency of the construction is given when the old cell volume is exactly filled by the new cell and the hexahedrons which represent the volume changes per

side, in other words when the outer surfaces with their diagonal orientation do not change and all inner surfaces common to two hexahedrons in figure 2 have the same diagonal direction when viewed from each of the neighbouring hexahedrons. This can easily be verified, all cellfaces with ξ, η and ζ normal direction have already globally common orientation of the surface diagonals, so that only the 12 surfaces common to two sweep-hexahedrons have to be controlled. Three of these surfaces with the common point 1' as well as the three with the common point 8 match the condition automatically, since the common point 1' and 8 is also the common starting point of the spatial diagonals of the neighbouring outer hexahedrons and, with the surface diagonals as projections of the spatial diagonal to the surfaces, the common starting point for the surface diagonals. The matching condition for the remaining 6 surfaces may now easily be verified manually.

The volume changes $(\Delta V)_j{}^{n+1}$ are now easy to calculate using the same hexahedron-partitioning into six tetrahedron as for the cell itself, adopting the spatial diagonal orientation according to the rules above. The normal cellface velocity fulfilling the GCL 2.11 is now calculated by:

$$\bar{v}_{g,j}^{n+1} = \frac{1}{\left|\vec{S}_j^{n+1}\right|} \sum_{m=n+2-k}^{n+1} b^m \frac{(\Delta V)_j{}^m}{\Delta t} \qquad (2.12)$$

2.2 Computational grids

To calculate the complete rotor configuration a chimera embedded overlapping grid technique is used [26]. The grid configuration for a 5-bladed Hughes 500 is shown in the following picture, 9 blocks for parallel calculation are used, 5 single block rotor grids, which mesh in the rotational symmetric basis grid composed of 4 blocks.
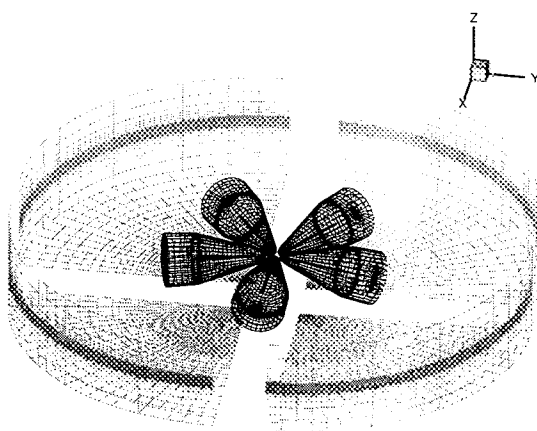

Figure 3: Chimera grid system for Hughes 500 rotor

To account for elastically deforming boundaries, dynamic grid blocks are introduced for the rotor grids. An efficient and robust 3-D algebraic grid deformation algorithm is used to update the positions of interior grid points with given new positions of the inner boundary points. The blade movement and elastic deformation is broken down into different parts, to be treated appropriately.

- The first part is a mean global translation and rotation, represented by a blade-root attached coordinate system $\{B_s\}$.
- The second part is a mean local translation, rotation and linear deformation for each spanwise section, represented by the translation vector u and the deformation gradient F with $x'=F\,x + u$.
- The third part is the remaining local deformation of each surface point with translation and rotation.

These 3 classes represent different deformation scales, their treatment in the algorithm is described in detail as follows:

The blade root attached secantial coordinate system $\{B_s\}$ describes a mean rigid body movement of the blade. Its y-axis is bound to the connection of the root and the tip reference point of the deformed blade, the z-direction is normal to the nose tail connection of the blade root. The outer grid boundary points are fixed in $\{B_s\}$, while the inner surface boundary points still move due to the elastic blade deformation. Without elastic deformation, the arbitrary movement of the rotor blade would only induce a corresponding movement of the rotor grid and could be handled by the chimera technique alone.

For the remaining elastic deformation in $\{B_s\}$, a mean translation vector u and deformation gradient $F(y)$ for each spanwise section is determined. Applying the linear mapping $x'=F\,x_{s,0} + u$ on the undeformed blade surface coordinates $x_{s,0}$ of the section leads to the virtual surface x' in $\{B_s\}$, which now includes a mean global translation and rotation as well as a mean translation rotation and linear deformation of each profile segment. For the mapping from $x_{s,0}$ to x_s', the translation of each surface point and the rotations of the surface normal are calculated. They are used as translations and slope changes of the ζ-grid lines normal to the body surface. Parametric hermit splines on the ζ-grid lines are used to calculate the relative translations of the interior grid points on this line, based on the translation and slope change of the body surface point as boundary condition. The parameter $g=g(\zeta)$ with $g=0$ at the body surface and $g=1$ at the outer boundary is chosen to be a linear function of the physical arc length along the grid line. For OH grid topologies with their degenerated cells at the tail, a special treatment of the first two or three grid points near the body surface with $\zeta < \zeta_g$ has to be

introduced to ensure a robust algorithm for larger deformations. We have introduced an intermediate grid layer $\zeta = \zeta g$ with a physical distance to the blade surface in the nose region of about 0.166 chordlengths. The translations and rotations of all grid points between the body surface and this intermediate grid layer are calculated by applying the linear mapping $x' = F\, x_0 + u$, while the interpolation algorithm with parametric hermit splines is applied to the grid region with $\zeta > \zeta g$. This avoids strong distortions of the profile tail cells.

With the given coordinates x_s of the deformed blade surface, the translations of each surface point and rotations of the surface normal are calculated for the mapping from x_s' to x_s. Once more an additional translation component of the inner grid points along the ζ-grid lines is calculated by using parametric hermit interpolation splines on the grid lines in computational space. This time for the interpolation of a local deformation, the parameter $g = g(\zeta)$ with $g=0$ at the body surface and $g=1$ at the outer boundary is chosen to be a linear function of the arc length in computational space.

The main idea of the algorithm is to break down the whole deformation in parts of different characteristic lengths. The smaller the characteristic length of the surface deformation, the more locally it will be propagated into the grid using the appropriate weighting function g, small scale surface deformations will only deform some grid cells in the close proximity. The algorithm is very efficient and sufficiently robust to handle the grid adaption for large deformations (see the following figure).
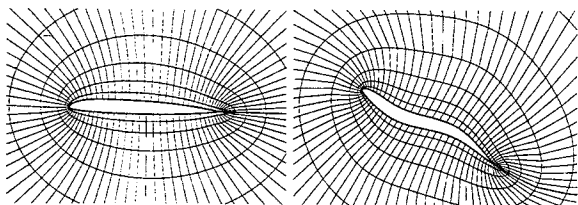

Figure 4: dynamic grid with algebraic algorithm

2.3 Structure calculation

The rotor system is modelled as a multibody system with rigid and elastic bodies in modal description, represented by their mass, damping and stiffness matrices. In the SIMPACK multibody simulation system, the equations of motion are solved by explicit time integration. For the Hughes 500, each rotor blade is modelled as an elastic beam in modal description with 4 elastic flap modes, 1 elastic bending mode and 4 elastic torsional modes.

2.4 Coupled scheme

The evolution of the fluid and structural domains is coupled over their common physical boundary, the body surface. The current highly unsteady fluid state defines, with its surface pressure forces, the boundary conditions of the structure dynamics, while the current structural state with the positions and velocities of the surface points determines the boundary conditions of the fluid state. One attempt to simulate this coupled problem numerically would be to solve at once one system of equations containing the structural as well as the aerodynamic degrees of freedom. Such an attempt may be feasible in certain simple cases. Problems arise for more complex configurations due to nonlinearities and different stiffness properties in the two domains, the problems may be unsolvable with existing experience and computing power. A further problem is that the vast experience in the numerical treatment of the fluid and structural domains adapted to their characteristic properties cannot be used.

A second attempt for the numerical solution of coupled systems, already commonly used for aeroelastic calculations, overcomes these shortcomings and allows a high degree of modularity for the coupled system. A time-marching staggered algorithm is used to solve the surface-coupled 2-field problem, where the fluid and structure domains are advanced from time n to n+1 independently by their own, well adapted numerical integration scheme. Surely, each domain has to be provided with the most current boundary information from the other domain before the integration process, the fluid domain has to be provided with boundary positions and velocities, the structural domain with current forces and moments.

Here some important choices can be made concerning the time level of the boundary data provided. Providing positions and velocities of time step n+1 to the fluid code to integrate from n to n+1 leads to an implicit treatment of this boundary data in the fluid integration scheme. When an implicit scheme is used for the fluid integration, this choice allows the consistent implicit treatment of all terms. Providing "older" fluid information of time step n leads to explicit treatment of the boundary terms. The same choice whether to use aerodynamic loads in an implicit or explicit manner must be made for the structural domain. Piperno [23] as well as Lesoinne and Farhat [19] showed that different schemes for the treatment of the boundary data may determine the stability limits and the accuracy of the coupled system. A general classification of different boundary treatment schemes for partitioned analysis can be found in [10].

An important criterion for the choice of the boundary treatment scheme is the impact on implementation costs

and software modularity. Explicit-explicit as well as the mixed implicit-explicit or explicit-implicit boundary treatments allow the integration of the coupled system by two staggered integrations in appropriate sequence, the calculation flow of each domain with one integration per time step is linear and identical to that of the uncoupled problem. Implicit-implicit boundary treatment may necessitate an iterative integration procedure where the fluid or the structure module has to perform more than one integration process per time step, which negatively affects modularity and computational costs. Here an implicit-explicit boundary treatment is used, which allows a simple and modular implementation consistent with the implicit fluid and explicit time integration scheme (Figure 5).
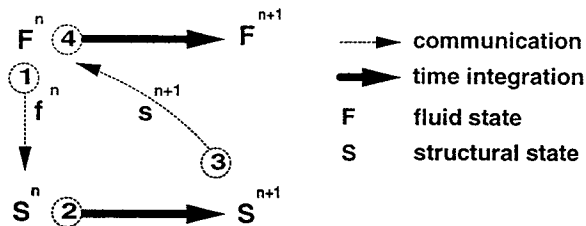
Figure 5: The used implicit-explicit coupling scheme

2.5 Implementation

Two separate codes, one for the aerodynamic and the other for the dynamic integration run on independent computer platforms, exchanging data over a TCP/IP socket connection. To get a high degree of modularity, a general interface description has been defined. At each time step, the fluid module must provide the aerodynamic force and moment vectors at the coupling control points. The structure module provides the kinematic blade root description with position vector, orientation matrix, velocity and angular velocity vector as well as the kinematic description set for each control point. This description set includes positions and velocities. Here, the velocities are included for generality reasons, they are not currently used in the aerodynamic module due to the velocity calculation by the GCL.

For the dynamic beam model used, the control points are located on the elastic axis of the blade with y-positions matching the η=const. planes of the aerodynamic grid. In addition to the positions and velocities at the control points, the orientation matrix and angular velocity are provided. The interface routine of the aerodynamic module instantly generates the new blade surface. The following steps are identical for a dynamic beam or surface model. They include the generation of the deformed 3-D rotor grids, the implicit time integration, the load calculation and the export of the aerodynamic loads at the control points to the dynamic module.

3 Results

3.1 Prescribed elastic deformation of a test rotor

Some calculations with prescribed elastic deformation of the rotor blade in hover and forward flight have been made. Figure 6 shows the z-component of the absolute aerodynamic blade lift over its azimuthal position for a helicopter in hover. In case 1 without flap, lag or elastically motion of the blade, a steady solution is reached, case 2 uses the same rotor with an additional Tip-Torsion of $\pm\,4°$ in the 5th harmonic while leaving the blade root fixed. Case 3 uses the same rotor, instead of the Tip-Torsion, we prescribe a variable Tip-Camber of $\pm\,3.5\%$ in the 5th harmonic while leaving the camber of the blade root fixed, a camber change that would lead to the same lift amplitude as the 4° torsion for a Joukowsky profile in incompressible flow.
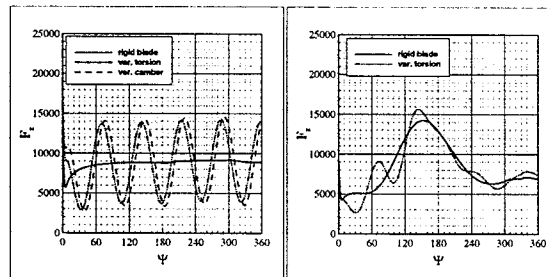

Fig. 6/7: Total blade lift of a test rotor in hover and 100 kt. forward flight with prescribed elastic deformation.

3.2 Hughes 500

The coupled aerodynamic – dynamic response of the Hughes 500 rotor configuration in Hover and 100 kt forward flight has been calculated. 49 control points on the elastic axis of each blade are used for the fluid-structure data exchange. Only the rigid flap mode and the first 4 elastic flap bending modes were considered. The two flight conditions considered are as follows:

Case		hover	100kt
Blade radius	[m]	4.05	4.05
Omega	[1/s]	51.836	51.836
Flight speed	[kt]	0	100
Advance ratio		0	0.25
Flight Mach number		0	0.1511
Tip Mach number		0.6167	0.6167
Shaft angle	[°]	0	-4.0

Table 2: Hughes 500 flight parameters

The results calculated will be compared with flight test data presented by Lindert [20]. There, the aerodynamic loads were derived from the measured structural response data by solving the inverse problem using a reconstruction method.

3.3 Trim calculation

For the two flight test cases, only rough collective pitch and no cyclic pitch angles at all was mentioned in [20], so a trim calculation with the coupled simulation model was performed to get a flap-angle distribution according to the flight test data. For the hover case, the collective pitch was used as trim parameter to obtain the measured mean flap angle. For the forward flight case, the collective pitch, the cyclic pitch amplitude and the phase angle of the cyclic pitch maximum were used as trim parameters, while the measured flap angle distribution was approximated by a harmonic distribution with the 3 parameters mean flap angle, flap angle amplitude and phase angle of the flap maximum. The trim calculation included the following steps: first, 3 revolutions with the coupled system were calculated to generate a nearly periodic dynamic and aerodynamic start solution. Then further trim revolutions with variations of the trim parameters were performed to determine the Jacobian matrix between these parameters and the parameters of the flap angle distribution and to reach the trimmed state by a Newton iteration. The trimmed pitch distribution at $r/R=0.7$ and the rough collective pitch values of the flight test are given in the following figure 8, the comparison between the calculated flap distribution and the measured values is given in the figures 9/10.
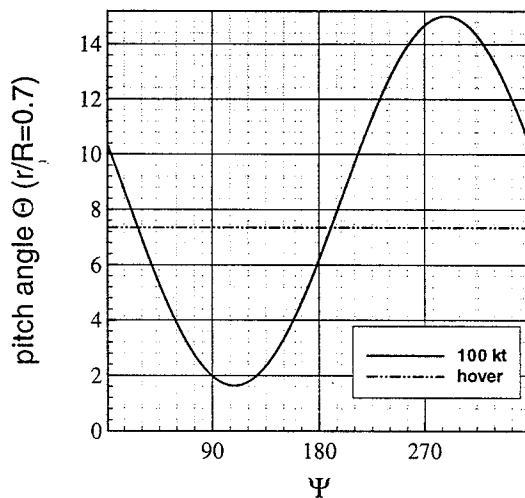

Figure 8: Pitch angle distribution for the trimmed cases

With $\Theta \approx \Theta_0 + \Theta_1 \cos(\Psi - \tau_\Theta)$	hover	100 kt
$\Theta_{\text{flight test}}$ [°]	≈7°	8-9°
Θ_0 [°]	7.3°	8.33°
Θ_1 [°]	0.0°	6.70°
τ_Θ [°]	0.0°	-71.5°

Table 3: Pitch angle parameters for the trimmed cases
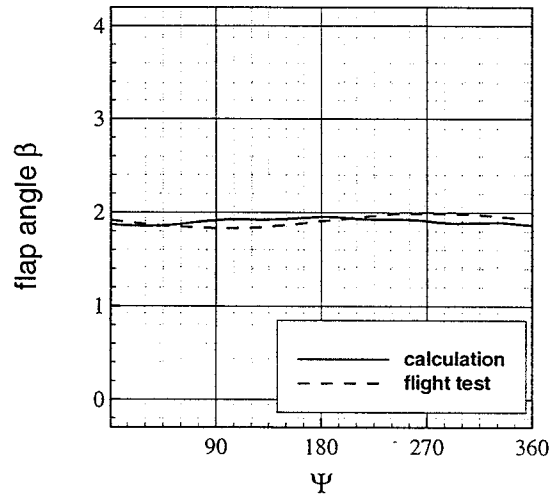

Figure 9: Calculated and measured flap angle in hover
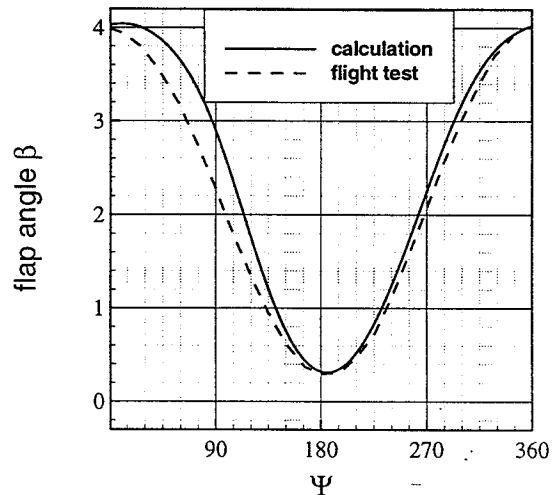

Figure 10: Calculated and measured flap angle in 100 kt forward flight

For the hover case, the coupled calculation will theoretically converge towards a constant flap angle due to the rotational symmetry of the rotor configuration where the fuselage and tail rotor influence is neglected. In the measured flight test data, this influence is evidenced in a slight asymmetric flap angle distribution.

3.4 Aerodynamic and elastic state of the hover case

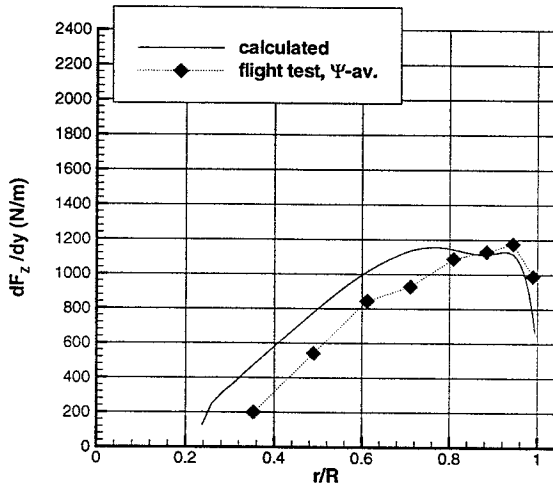The spanwise blade load distribution is shown in the following figure 11.

Figure 11: Spanwise load distribution in hover

The results calculated are shown for the 6. revolution after the start from initial conditions of undisturbed flow.

Comparing the flight test load distribution with the calculated distribution, we have to remember that the flight test data was not measured directly by pressure measurement. Instead, absolute forces at the control points were reconstructed from measured structural deformations and an average load distribution was calculated with the assumption of piecewise constant loads.
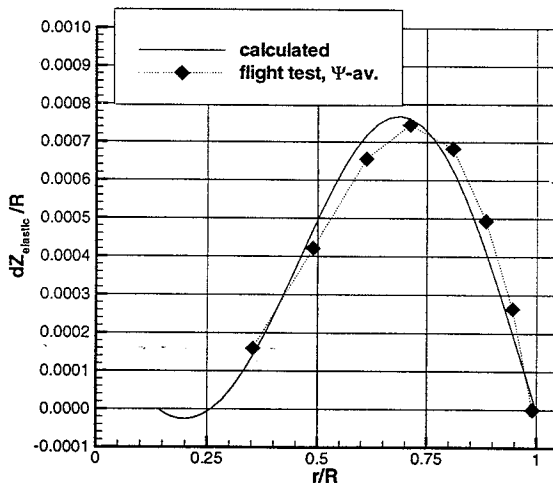
Fig. 12: Spanwise elastic deformation in hover

The elastic blade bending deformations of the calculation and the flight test, shown in figure 12, are in good correspondence.

3.5 Aerodynamic and elastic state of the 100 kt case

For the 100 kt forward flight case, the vortex structure, the load distributions and the elastic deformations are given in the following figures 13-15.
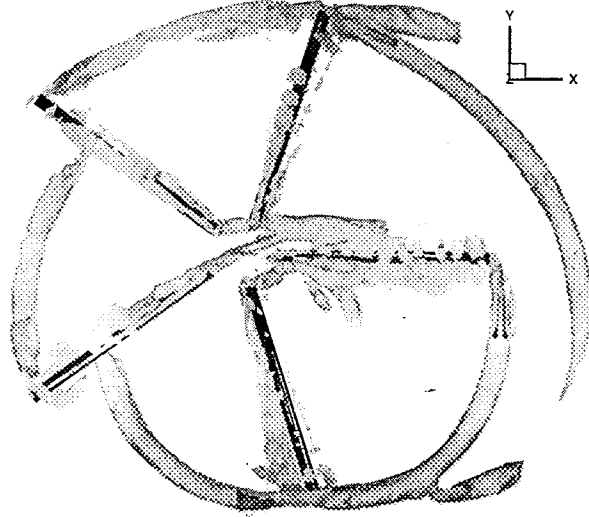
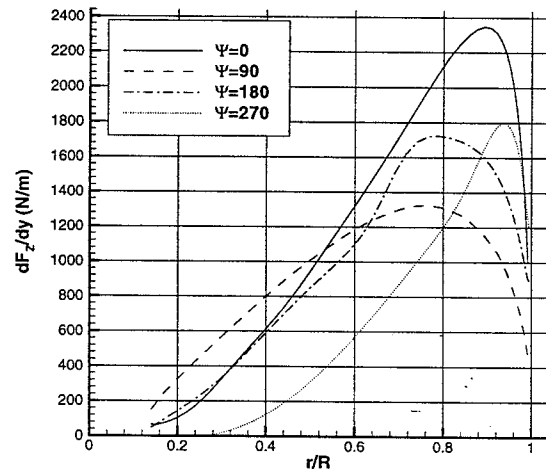**Figure 13:** Vortex structure for the 100 kt case

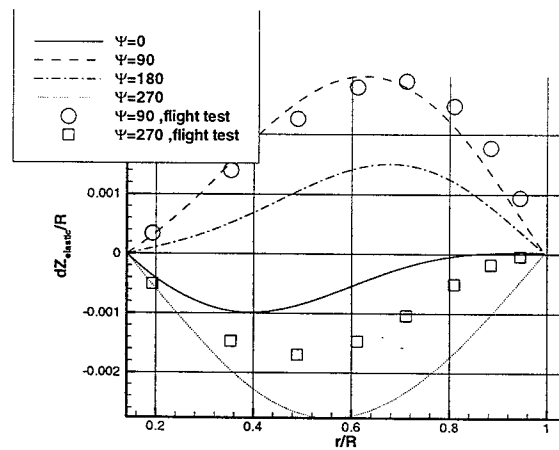**Figure 14:** Spanwise load distribution, 100 kt

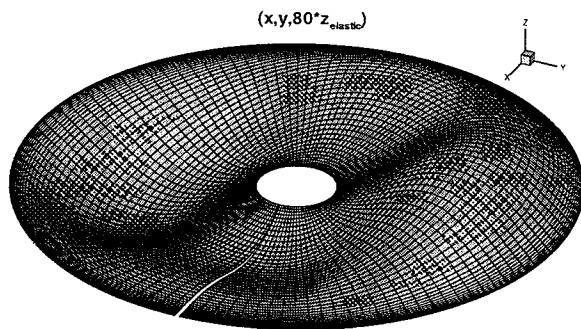**Figure 15:** Spanwise elastic deformation, 100 kt

Figure 16: Elastic deformation, 100 kt

A direct comparison of calculation and flight test data for the 100 kt case should be undertaken with caution. On one hand, not all necessary forward flight parameters of the flight test were given in [20]. In fact, neither the shaft angle, nor the pitch control angles were given. For the shaft angle, a value of –4° was assumed, and the trim procedure was performed to get the pitch angles. On the other hand, our simulation model cannot account for the influence of the fuselage and tail rotor, and the lag and torsional degrees of freedom, which are important in the forward flight case, are not yet activated in the calculation presented. Because of the unknown shaft angle and the influence of the fuselage and tail rotor it is especially difficult to compare the data sets in the 0° and 180° azimuthal positions, so the flight test comparison is only shown for the deformations in lateral azimuthal blade positions.

4 Conclusions

We have presented a simulation model for the aeroelastic analysis of helicopter rotors. To solve the task of coupled aeroelastic calculations for the given complex application with multiple flexible rotor blades in relative motion and a transonic, unsteady flow, a highly modular partitioned procedures approach with a time-marching "staggered solution" scheme was chosen. The fluid domain is described by the Euler equations in an ALE formulation, and a finite volume upwind flow solver with chimera grid technique is used to solve the equations numerically. The geometric conservation law for the implicit time integration scheme of first, second or third order of time accuracy was applied. An efficient and robust algebraic 3-D grid deformation algorithm for the structured blade grids was developed. For the dynamic modelling, a multibody simulation system was used, which allows the representation of the rotor blades as elastic beam or FEM model, the fluid and structural modules are coupled via a subiteration free implicit-explicit staggered scheme, allowing a highly modular design.

Calculations of the aeroelastic behaviour of the 5-bladed Hughes 500 rotor in hover and 100 kt forward flight

were presented, with the flap motion and the first 4 flap bending modes considered as dynamic degrees of freedom. In both cases, a trim calculation with the coupled simulation system was performed and the aerodynamic loads and structural deformations were determined. While the flight test data available for the 100 kt case allows only cautious qualitative comparison, a closer comparison with measured load and deformation data is possible for the hover case. This comparison shows good qualitative and quantitative accordance between computed and measured flight test data. The next calculations will include lag and torsional modes of freedom. Further investigation should include different integration schemes for the structural domain and different coupling schemes with special focus on stability and accuracy.

References

[1] Ballhaus, W.F. and Goorjian, P.M., "Computation of Unsteady Transonic Flows by the Indicial Method", AIAA Journal, Vol. 16, 1978, pp. 117-124

[2] Batina, J.T.; Seidel, D. A.; Bland, S. R.; Bennett, R. M., "Unsteady Transonic Flow Calculations for Realistic Aircraft Configurations", Journal of Aircraft, Vol. 26, No. 1, 1989, pp. 21-28

[3] Batina, J.T., "Unsteady Euler Algorithm with Unstructured Dynamic Mesh for Complex-Aircraft Aerodynamic Analysis", AIAA-Journal, Vol. 29, No. 3, 1991, pp. 327-333

[4] Brenneis, A, "Berechnung instationärer zwei-und dreidimensionaler Strömungen um Tragflügel mittels eines impliziten Relaxationsverfahrens zur Lösung der Eulergleichungen", PhD thesis, Universität der Bundeswehr München, VDI-Fortschrittsberichte, Reihe 7, Nr. 165, 1989, VDI-Verlag, Düsseldorf

[5] Demirdzic, I; Peric, M, "Space Conservation Law in Finite Volume Calculations of Fluid Flow", International Journal for Numerical Methods in Fluids, Vol. 8, 1037-1050 (1988)

[6] Eberle A., "MBB-EUFLEX. A new Flux extrapolation scheme Solving the Euler Equations for Arbitrary 3-D Geometry and Speed.", Bericht MBB/LKE122/S/PUB/140,MBB, Germany, 1984

[7] Edwards, J.W.; Bennett, R.M. ; Whitlow, W. Jr. and Seidel, "Time-marching transonic Flutter Solutions Including Angle of Attack Effects", Journal of Aircraft, Vol. 20, No. 11, 1983, pp. 899-906

[8] Edwards, J.W.; Malone, J.B., "Current status of computational methods for transonic unsteady aerodynamics and aeroelastic applications", Comp. Systems in Engineering, Vol. 3, 1992, No. 5, pp.545-569

[9] Farhat, C.; Lesoinne, M.; Chen, P.S.; Lanteri, S., " Parallel heterogeneous algorithms for the solution of three-dimensional transient coupled aeroelastic problems", AIAA/ASME/ASCE/AHS Structures, Structural Dynamics & Materials Conference - Collection of Technical Papers Vol. 2, 1995. AIAA, New York, USA. pp. 1146-1160

[10] Felippa, C.A.; Geers, T. L., "Partitioned Analysis for Coupled Mechanical Systems", Engineering Computations, Vol. 5, 1988, pp. 123-133

[11] Guruswamy, G.P.; Yang, T. Y.;, "Aeroelastic Time Response Analysis of Thin Airfoil by Transonic Code LTRAN2", Computers and fluids, Vol. 9, No. 4, 1980, pp. 409-425

[12] Guruswamy, G.P., "Time Accurate Unsteady Aerodynamic and Aeroelastic Calculations of Wings Using Euler Equations", AIAA-Paper 88-2281, 1988

[13] Guruswamy, G.P.; Obayashi, S., "Transonic Aeroelastic Computations on Wings Using Navier-Stokes equations", AGARD CP-507, Oct. 1991, No. 22

[14] Kutler P., "Multidisciplinary computational aerosciences", Computing Systems in Engineering, Vol.3, No 1-4, 1992, pp. 87-95

[15] Krämer, E.; Hertel, J.; Wagner, S., "Euler Procedure for Calculation of the Steady Rotor Flow with Emphasis on Wake Evolution", AIAA Paper 90-3007, presented at the AIAA 8th Applied Aerodynamics Conference, Portland, OR, August 20-22, 1990

[16] Krämer, E., "Theoretische Untersuchungen der stationären Rotorblattumströmung mit Hilfe eines Euler-Verfahrens", PhD thesis, Universität der Bundeswehr München, VDI-Fortschrittsberichte, Reihe 7, Nr. 197, 1991, VDI-Verlag, Düsseldorf

[17] Lesoinne, M.; Farhat, C., "Geometric conservation law for aeroelastic computations Using unstructured dynamic meshes", AIAA-Paper No. 95-1709, 1995

[18] Lesoinne, M.; Farhat, C., "Geometric conservation laws for flow-problems with moving boundaries and deformable meshes, and their impact on aeroelastic computations", Computer methods in applied mech. and engineering, Vol. 134, 1996, pp. 71-90

[19] Lesoinne, M.; Farhat, C., "Improved staggered algorithms for the serial and parallel solution of three-dimensional nonlinear transient aerolelastic problems", Proceedings of the World Conference on Computational Mechanics IV, edited by Onate and Idelsohn, Barcelona, Spain 1998 (to appear)

[20] Lindert, H.W., "Anwendung einer strukturmechanischen Methode zur Rekonstruktion der Luftkräfte am rotierenden Rotorblatt aus Windkanal- und Flugversuchsmessungen", PhD thesis, RWTH Aachen, VDI-Fortschrittsberichte, Reihe 12, Nr. 245, 1994, VDI-Verlag, Düsseldorf

[21] NKonga, B., "Godunov type method on non-structured meshes for three dimensional moving boundary problems", Computer Methods in Applied Mech. and Engineering, Vol. 113, 1994, pp. 183-204

[22] Obayashi, S; Guruswamy, G. P.; Goorjian, P. M., "Streamwise Upwind Algorithm for Computing Unsteady Transonic Flows Past Oscillating Wings", AIAA Journal, 1991, Vol. 29, No. 10, pp. 1668-1677

[23] Piperno, S.; Farhat, C.; Larrouturou, B., "Partitioned procedures for the transient solution of coupled aeroelastic problems part I: model problem, theory and two-dimensional application", Computer Methods in Applied Mechanics and Engineering Vol. 124 no. 1-2 June 15 1995, pp. 79-112

[24] Piperno, S., "Simulation numerique de phénomènes d' interaction fluide-structure", Dissertation thesis, L'école nationale des ponts et chaussées, France, June 1995

[25] Rizzetta, D.P., "Time-Dependent Response of a Two-Dimensional Airfoil in Transonic Flow", AIAA Journal, Vol. 17, 1979, pp. 26-32

[26] Stangl, R.; Wagner, S., " Euler Simulation of a Helicopter Configuration in Forward Flight using a Chimera Technique", Presented at the American Helicopter Society 52nd Annual Forum Washington D.C., June 4-6, 1996

[27] Thomas P.D., Lombard C.K., "Geometric conservation law and its application to flow computations on moving grids", AIAA Journal, Vol. 17, 1979, pp. 1030-1037

[28] Trepanier, J.Y., Reggio, M.; Zhang, H.; Camarero, R., "A Finite Volume Method for the Euler Equations on Arbitrary Lagrangian-Eulerian Grids", Computers and Fluids, Vol.20, No. 4, 1991, pp. 399-409

[29] Vinokur, M., "An Analysis of Finite-Difference and Finite-Volume Formulations of Conservation Laws", Journal of Computational Physics, Vol. 81, pages 1-54, 1989

[30] Wehr, D.; Zerle, L.; Wagner, S., " Coupling Euler and Potential Methods for Rotors in Unsteady Forward Flight", Proceedings of the 22nd European Rotorcraft Forum, Brighton, Paper no. 59, 1996

[31] Zhang, H.; Reggio, M.; Trepanier, J. Y.; Camarero, R., "Discrete Form of the CGL for Moving Meshes and Its Implementation in CFD Schemes", Computers and Fluids, Vol.22, No. 1, 1993, pp. 9-23